

Nearby boundaries create eddies near microscopic filter feeders

Rachel E. Pepper¹, Marcus Roper^{2,3}, Sangjin Ryu⁴,
Paul Matsudaira⁵ and Howard A. Stone^{6,*}

¹*Department of Physics, Harvard University, Cambridge, MA 02138, USA*

²*Department of Mathematics, and* ³*Lawrence Berkeley National Laboratory, University of California, Berkeley, CA 94720, USA*

⁴*Department of Mechanical Engineering, Massachusetts Institute of Technology, Cambridge, MA 02139, USA*

⁵*Department of Biological Sciences, National University of Singapore, Singapore 117543, Republic of Singapore*

⁶*Department of Mechanical and Aerospace Engineering, Princeton University, Princeton, NJ 08544, USA*

We show through calculations, simulations and experiments that the eddies often observed near sessile filter feeders are frequently due to the presence of nearby boundaries. We model the common filter feeder *Vorticella*, which is approximately 50 μm across and which feeds by removing bacteria from ocean or pond water that it draws towards itself. We use both an analytical stokeslet model and a Brinkman flow approximation that exploits the narrow-gap geometry to predict the size of the eddy caused by two parallel no-slip boundaries that represent the slides between which experimental observations are often made. We also use three-dimensional finite-element simulations to fully solve for the flow around a model *Vorticella* and analyse the influence of multiple nearby boundaries. Additionally, we track particles around live feeding *Vorticella* in order to determine the experimental flow field. Our models are in good agreement both with each other and with experiments. We also provide approximate equations to predict the experimental eddy sizes owing to boundaries both for the case of a filter feeder between two slides and for the case of a filter feeder attached to a perpendicular surface between two slides.

Keywords: biofluids; filter feeder; *Vorticella*; Brinkman; stokeslet; boundaries

1. INTRODUCTION

Microscopic sessile filter feeders are an important part of aquatic ecosystems and form a vital link in the transfer of carbon in marine food webs (Fenchel 1982; Sherr & Sherr 1988; Christensen-Dalsgaard & Fenchel 2003; King 2005). The filter feeders consume bacteria and small detritus, and are in turn eaten by larger organisms. Sessile filter feeders live in bodies of water where they are anchored to the stream or ocean bed, aquatic plants or even aquatic animals (Laybourn 1976; Kankaala & Eloranta 1987). They survive by creating a feeding current that draws fluid towards them, and from which they filter their food of interest. These organisms also play an important role in biological waste water treatment (Reid 1969; Chen *et al.* 2004). An understanding of the flow generated by filter feeders may enable not only a better understanding of marine ecology and carbon cycling, but also improvement of water treatment plant design.

Sessile filter feeders typically have a cell body with a radius ranging from a few to a few hundred microns, and

are typically attached either directly or with a stalk to an immobile surface (e.g. an aquatic plant). Some common sessile filter feeders are *Vorticella* (Sleigh & Barlow 1976), *Stentor* (Rapport *et al.* 1972) and choanoflagellates (King 2005). We will focus on *Vorticella* as a typical sessile filter feeder. *Vorticella* are a stalked protozoan with a bell-shaped cell body approximately 25 μm across and approximately 50 μm long (Noland & Finley 1931). This body is attached to a surface via a thin stalk of length about 100 μm . *Vorticella* create a feeding current using a ring of beating cilia at the top of their body, and use two rings of cilia to filter debris from the surrounding fluid (Sleigh & Barlow 1976). The debris can then be ingested into the cell body or rejected into the surrounding fluid (Sleigh & Barlow 1976). There are several possible mechanisms for such particle capture (Rubenstein & Koehl 1977; Labarbera 1984).

Experimental observations of several different sessile filter feeders have shown that they generate feeding currents in the form of a toroidal vortex (Sleigh & Aiello 1972; Sleigh & Barlow 1976; Pettitt *et al.* 2002; Hartmann *et al.* 2007; Petermeier *et al.* 2007; Nagai *et al.* 2009). Closed feeding streamlines limit the feeder's

*Author for correspondence (hastone@princeton.edu).

access to new material (Blake & Otto 1996), so it is important to determine what circumstances lead to closed eddies. The eddy structure is typically attributed to the substrate to which the organism is attached. For instance, Blake & Otto (1996) modelled the feeding eddy structure as a point force, or stokeslet, oriented perpendicular to a plane wall, and this model has been used to estimate feeding fluxes in several biological contexts (Pettitt *et al.* 2002; Orme *et al.* 2003; Hartmann *et al.* 2007).

However, eddies have also been observed near filter feeders even in the absence of a tethering substrate, for instance for a *Vorticella* attached to a thin strand of duckweed (Sleigh & Barlow 1976) or anchored between two closely spaced parallel slides (Nagai *et al.* 2009). It seems little recognized that the eddies in these situations, and in fact in the majority of observations of microorganisms, are probably a result of confinement between two walls parallel to the field of view, e.g. the two microscope slides that are nearly universally present when experimentally examining microorganisms (Liron & Blake 1981; Blake *et al.* 1982).

Liron & Blake (1981) have shown through calculations that closed eddies form only in the presence of boundaries and based on their theoretical calculations suggested that the flow near sessile micro-organisms is mostly determined by the container geometry. They model point-force-generated feeding currents in several geometries, including a stokeslet between two infinite parallel plane boundaries with the stokeslet oriented parallel to the boundaries (Liron & Blake 1981). However, it is difficult to confirm the existence or non-existence of such eddies experimentally, as it is not possible to observe filter feeders under a microscope without introducing at least one nearby boundary.

We build on the calculations of Liron & Blake (1981), and extend them to more complex models of micro-organisms to make experimentally verifiable predictions. We find that the size of the eddies increases approximately linearly with the distance between the confining slides, and emphasize that, according to our calculations and simulations, the eddies disappear entirely for the case of a filter feeder in free space. We then present what we believe is the first experimental confirmation that eddies near filter feeders are due to the boundaries provided by the surrounding slides by showing that the eddy size increases as predicted as the distance between the two confining slides is increased. The origin of these eddies must be taken into account when explaining microscopic filter feeding, as the flow around filter feeders in nature will be quite different from that when examined under a microscope between two slides. We also anticipate that the surroundings of filter feeders, such as whether they have nearby neighbours, will strongly affect the flow nearby, and thus the filter feeder's access to food, oxygen and other nutrients.

2. STOKESLET BETWEEN TWO WALLS

It is common to model sessile filter feeders (and micro-organisms for which gravity is significant) as a point

Table 1. List of symbols used in the main body text in order of appearance.

symbol	physical meaning
r	radial coordinate in cylindrical coordinates
h	distance between no-slip walls in the z direction in experiment, simulation and theory
μ	liquid viscosity
\mathbf{u}	liquid velocity field
p	liquid pressure field
r_{sp}	distance between the origin (centre of forcing) and the eddy centre
a	radius of living or model <i>Vorticella</i> depending on context
θ	polar coordinate in cylindrical or spherical coordinates depending on context
ϑ	the co-latitude in cylindrical coordinates $\vartheta = \pi - \theta$
k	permeability used in Brinkman approximation
β	proportionality constant in the definition of k
γ_E	Euler–Mascheroni constant
ρ	radial coordinate in spherical coordinates
w	width of chamber in simulations
b	length of chamber in simulations
ℓ_{st}	the length of the <i>Vorticella</i> stalk
r_{sp}^j	the eddy size for a sphere located above a single plane boundary

force in Stokes flow—the stokeslet (Blake & Otto 1996; Hartmann *et al.* 2007; Drescher *et al.* 2009). Micro-organisms that swim generally do not exert a net force on the surrounding fluid, as the force generated by cilia for swimming is balanced by drag on the organism. However, sessile organisms can apply a net force to the fluid as they are attached (often via a stalk) to a substrate. It is therefore reasonable to approximate such sessile filter feeders using a stokeslet. As the velocity from the stokeslet in free space decays as $1/r$, where r is the distance from the stokeslet, and corrections from the details of the body shape and distribution of cilia decay as $1/r^2$ or more rapidly, the stokeslet approximation is likely to be valid far away from the organism. However, if eddies are present in the flow, then their structure may be sensitive to details of the flow close to the organism. In particular, we consider the position of the centre of the eddy, which may be quite close to the organism. It is not clear that a stokeslet model will correctly describe this near-body flow. Here, we compute the position of the stagnation point for a stokeslet between parallel walls, a distance h apart, and in later sections compare it with more realistic models of a filter feeder as well as with experimental results. Note that a list of relevant symbols and their meanings can be found in table 1.

To calculate the flow field, we solve the incompressible Stokes equation and the continuity equation

$$\mu \nabla^2 \mathbf{u} = \nabla p \quad \text{and} \quad \nabla \cdot \mathbf{u} = 0. \quad (2.1)$$

We follow Mucha *et al.* (2004) to numerically calculate the velocity field due to a stokeslet between and parallel to two no-slip walls. For ease of calculation and without affecting the flow near the stokeslet, periodic boundary

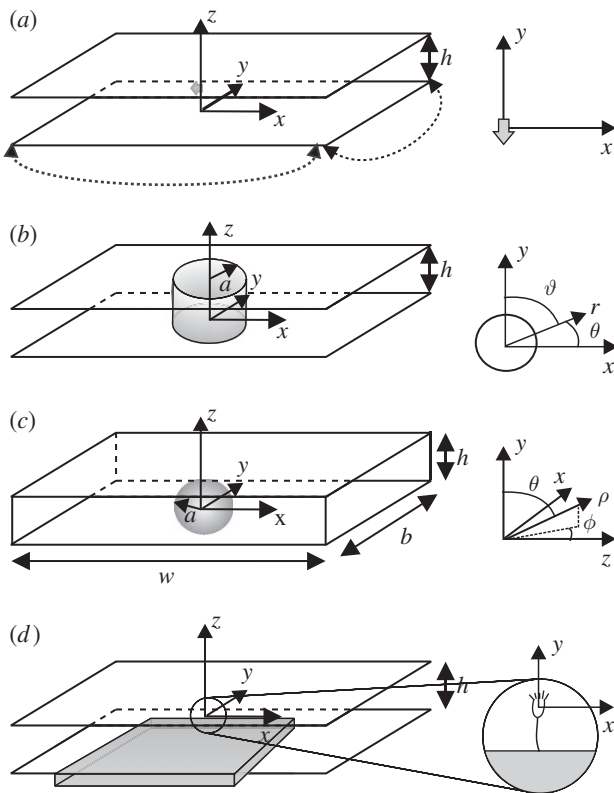


Figure 1. (a) Stokeslet between parallel walls. The stokeslet is represented by a grey arrow pointing in the $-e_y$ direction and the dotted lines represent periodic boundaries. The upper and lower boundaries (parallel to the $x-y$ plane) are no-slip. (b) Brinkman approximation geometry. (c) Simulation geometry. The upper and lower boundaries are no-slip. The right-hand and left-hand boundaries are open, and the front and back boundaries are slip. (d) A schematic view of the experimental set-up. *Vorticella* are grown on the narrow edge of a glass coverslip (grey box), which is inserted midway between two slides, a distance h apart.

conditions are imposed on pairs of control surfaces orthogonal to the bounding walls and far from the stokeslet (see figure 1a for a schematic view). We set the width and length of the periodic boundaries (in the x and y directions) to be much larger than the distance, h , between the no-slip walls, such that the eddy structure is determined by the no-slip walls. The stokeslet is located in the mid-plane at $(0, 0, h/2)$ and points in the $-e_y$ direction. Details of the calculation are found in appendix A. We note that an alternative calculation for a stokeslet between infinite parallel walls can be found in Liron & Mochon (1976).

Previous discussions of the eddies generated by a stokeslet between parallel plates have approximated the flow as generated by a potential dipole (Liron & Blake 1981; Blake *et al.* 1982). In this limit, it is not possible to make an approximation for the position of the eddy centres, as for a point dipole all streamlines share a common tangent at the position of the dipole, and both eddy centres are located at the position of the dipole. Instead of making such an approximation, we calculate the full solution to the Stokes equation in the near field. This approach allows us to find the position of the centre of the eddy. The flow is symmetric

around the axis of the stokeslet (figure 2a), such that the stagnation point at the centre of the eddy in the $z = h/2$ plane is located on the x -axis. As all length scales can be non-dimensionalized by h , we find that the distance to the stagnation point, r_{sp} , at the centre of the eddy increases linearly with the distance between the no-slip plane boundaries. In fact, from the numerically computed streamlines near the stokeslet (figure 2), we find $r_{sp}/h = 0.44 \pm 0.01$.

3. BRINKMAN APPROXIMATION

The stokeslet approximation described in §2 does not take the finite size of the feeding organism into account, or the distribution of the cilia that maintain continuous circulation of the fluid. The detailed geometry of the cell body may significantly affect the flow field near to the organism (Sleigh & Aiello 1972). In this section, we exploit the narrow-gap geometry of the feeding currents to introduce an approximation that can handle the finite-sized cell body.

We treat the feeding organism as a cylinder, of radius a , between two closely spaced walls as shown in figure 1b. For ease of comparison, rather than using the customary polar coordinate angle θ , we define the co-latitude $\vartheta = \pi - \theta$ (figure 1b), and write all equations of motion in terms of r and ϑ . Together, r , ϑ and $-z$ form a right-handed coordinate system. We model the generation of a feeding current by cilia distributed over the cell body by prescribing a tangential velocity u_ϑ . A similar method of prescribing tangential velocity has been used to model swimming microorganisms (Magar *et al.* 2003; Ishikawa & Pedley 2008). Surface-generated flows around swimming *Volvox* have been represented in a functionally similar manner using a prescribed tangential stress boundary condition (Short *et al.* 2006). In order to show the effect of the distribution of cilia on the cell body upon the flow streamlines, we consider two different velocity distributions at $r = a$ (figure 3). The first, or symmetric, model has $u_\vartheta = u_0 \sin \vartheta$ at $r = a$, which we assume models a symmetric distribution of cilia on the surface pushing fluid tangentially with typical speed u_0 . The second type of boundary condition is intended to capture the fact that cilia are concentrated near the top of the organism in a ‘crown’, as is true of many filter feeders, including *Vorticella*. For this asymmetric model, we have at $r = a$

$$u_\vartheta = \begin{cases} u_0 e^{-(\cos(\vartheta)-c)^4/d} & 0 < \vartheta \leq \pi, \\ -u_0 e^{-(\cos(\vartheta)-c)^4/d} & \pi < \vartheta \leq 2\pi, \end{cases} \quad (3.1)$$

where we choose $c = 1/2$ and $d = 1/100$ to provide a localized surface forcing and where variables are dimensional for the moment. The two cases account for the change in direction of e_ϑ so that the final velocity is symmetric across the y -axis. In both models, $u_r = 0$ at $r = a$ so that there is no flow through the cylinder surface.

To calculate the flow, we solve equation (2.1) non-dimensionalized by scaling all lengths by a , velocities

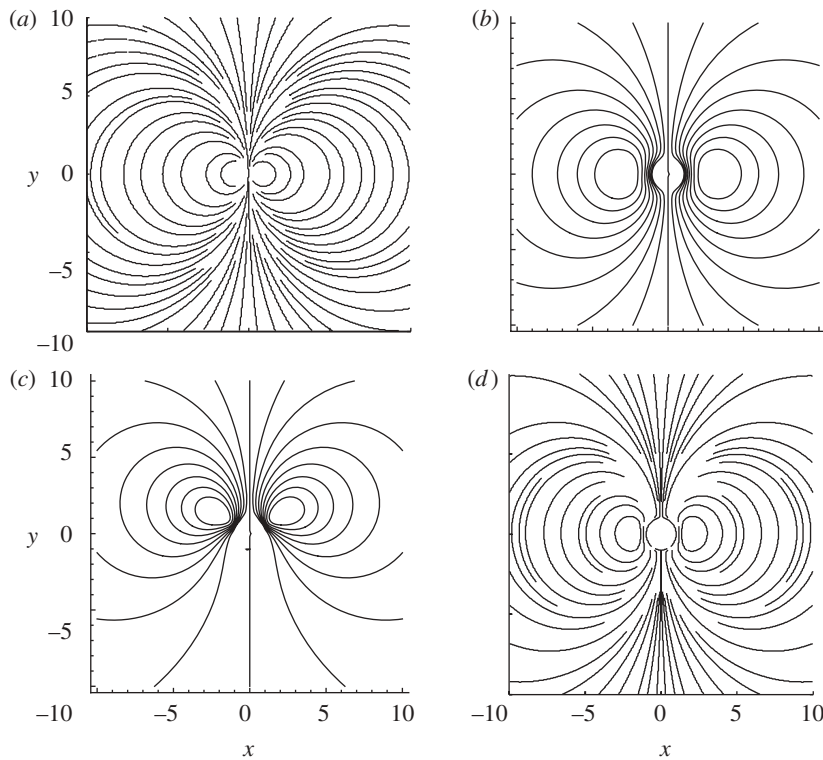


Figure 2. Streamlines in the mid-plane for different filter-feeder models. (a) Stokeslet model from §2 scaled by h . (b) Brinkman symmetric model from §3 with $h = 2.5a$ and $k = (h/a)^2$. (c) Brinkman asymmetric model from §3 with $h = 2.5a$ and $k = (h/a)^2$. (d) Simulation from §4 with $h = 2.5a$.

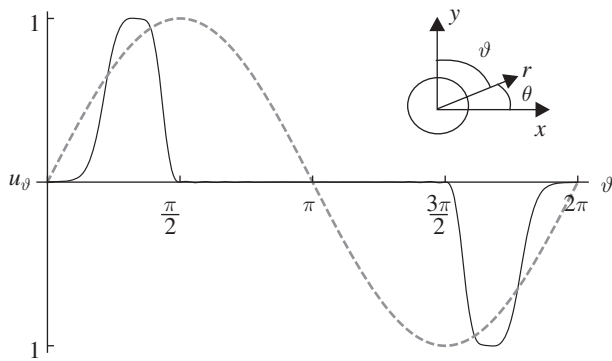


Figure 3. The non-dimensional velocity, u_ϑ , at $r = 1$, the surface of the cylinder, for the symmetric (dashed line) and asymmetric (solid line) Brinkman models.

by u_0 and stresses by $\mu u_0/a$. We also specify $\mathbf{u} = e_\vartheta u_\vartheta$ on $r = 1$ and no-slip conditions on all other rigid boundaries ($z = \pm (1/2)(h/a)$), with the flow vanishing at infinity. Finally, we work under the Brinkman approximation (Brinkman 1947; Tsay & Weinbaum 1991; Fernandez *et al.* 2002) for the variation of the flow across the gap, which gives: $\partial^2 \mathbf{u} / \partial z^2 = -(\mathbf{u}/k)$, where $k \propto (h/a)^2$ is the permeability, and the velocity is restricted to planes parallel to the boundaries, i.e. $\mathbf{u} = (u_r, u_\vartheta)$ and $u_z \equiv 0$. In addition to modifying the usual Hele–Shaw flow law to include the viscous effect of flow variations parallel to the cover slips (Fernandez *et al.* 2002), the Brinkman approximation allows both normal and tangential velocity boundary conditions to be applied on the surface

of the cylinder. We expect that the velocity decays as $r \rightarrow \infty$. The r and ϑ components of this equation give, respectively,

$$\frac{\partial p}{\partial r} = \frac{\partial}{\partial r} \left(\frac{1}{r} \frac{\partial}{\partial r} (r u_r) \right) + \frac{1}{r^2} \frac{\partial^2 u_r}{\partial \vartheta^2} - \frac{2}{r^2} \frac{\partial u_\vartheta}{\partial \vartheta} - \frac{u_r}{k} \quad (3.2)$$

and

$$\frac{1}{r} \frac{\partial p}{\partial \vartheta} = \frac{\partial}{\partial r} \left(\frac{1}{r} \frac{\partial}{\partial r} (r u_\vartheta) \right) + \frac{1}{r^2} \frac{\partial^2 u_\vartheta}{\partial \vartheta^2} + \frac{2}{r^2} \frac{\partial u_r}{\partial \vartheta} - \frac{u_\vartheta}{k}, \quad (3.3)$$

and the continuity equation is

$$0 = \frac{1}{r} \frac{\partial}{\partial r} (r u_r) + \frac{1}{r} \frac{\partial u_\vartheta}{\partial \vartheta}. \quad (3.4)$$

In appendix B, we derive the general solution to this system of equations. In particular, given the generic boundary condition $u_\vartheta = \sin n\vartheta$ on the surface of the cylinder, the velocity and pressure fields take the form

$$\left. \begin{aligned} u_r(r, \vartheta) &= \left(\frac{c_2}{r^{n+1}} + \frac{c_3}{r} K_n \left(\frac{r}{\sqrt{k}} \right) \right) \cos n\vartheta, \\ u_\vartheta(r, \vartheta) &= \left(\frac{c_2}{r^{n+1}} + \frac{c_3}{r} \left[K_n \left(\frac{r}{\sqrt{k}} \right) + \frac{r}{n\sqrt{k}} K_{n-1} \left(\frac{r}{\sqrt{k}} \right) \right] \right) \sin n\vartheta \\ \text{and } p(r, \vartheta) &= \frac{c_2}{knr^n} \cos n\vartheta, \end{aligned} \right\} \quad (3.5)$$

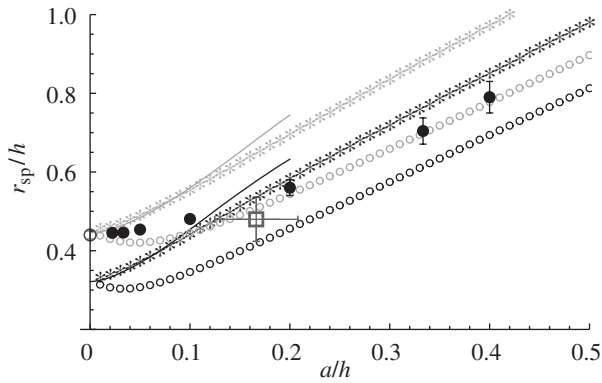


Figure 4. Eddy size for several different models of a filter feeder. Large open circle (white), stokeslet between parallel plates. Asterisks, Brinkman symmetric model; open circles, Brinkman asymmetric model; solid line, Brinkman symmetric model expansion as detailed in the text for $a/h \rightarrow 0$. For the Brinkman model, grey symbols correspond to the best fit value $\beta = 0.16$ and black to the Hele–Shaw approximation $\beta = 1/12$. Filled circles, three-dimensional simulation (§4). Open rectangle (dark grey), experimental observations; error bars show 95% confidence interval.

where K_n are the modified Bessel functions of the second kind and, for some pair of constants c_2 and c_3 , that must be determined from the boundary conditions. At $r = 1$, we have $u_r = 0$ and $u_\vartheta = \sin n\vartheta$ for all ϑ and k . Hence, we find

$$c_3 = -\frac{c_2}{K_n(1/\sqrt{k})} \quad \text{and} \quad c_2 = -\frac{n\sqrt{k}K_n(1/\sqrt{k})}{K_{n-1}(1/\sqrt{k})}. \quad (3.6)$$

Setting $n = 1$ in equations (3.5) and (3.6) gives a solution for the symmetric model filter feeders.

To create the ‘crown of cilia’ boundary condition, we use a Fourier series $u_\vartheta = \sum_1^\infty A_n \sin(n\vartheta)$ with $A_n = (2/\pi) \int_0^\pi e^{-(\cos(\vartheta) - c)^4/d} \sin(n\vartheta) d\vartheta$ with c and d as defined earlier. We find that 25 terms in this series are required to limit error in the boundary condition to less than 1 per cent (the 25-term sum is plotted in figure 3). Streamlines for both cases are shown in figure 2.

We define the size of the eddy, r_{sp} , as the distance from the centre of the cylinder to the stagnation point at the centre of the eddy (scaled by a). This distance is numerically calculated by finding the point where $u_\vartheta = u_r = 0$. In the symmetric case, this point falls on the x -axis ($\vartheta = \pi/2$). In both cases, the eddy size increases with the spacing between the confining walls (see figure 4 where we have now scaled r_{sp} by h rather than a). To determine the dependence of eddy size upon the gap width, we define $k = \beta(h/a)^2$, where β is a proportionality constant. We plot the cases $\beta = 1/12$ in figure 4, which is the value for pressure-driven flow in a Hele–Shaw cell without obstacles and also the case $\beta = 0.16$, which gives an exact match between the value for r_{sp} for the stokeslet and the asymptotic value of r_{sp} in the Brinkman geometry at $a/h = 0$. We can analytically evaluate the contribution of the finite-sized cell body to the size of the eddy when $h \gg a$. For large k , asymptotic analysis (appendix B) gives $r_{\text{sp}}/h = 1.114\sqrt{\beta} + 1.14\beta^{-1/2}$

$[1 - 2\gamma_E - 2\ln(a/(2\sqrt{\beta}h))](a/h)^2$, where γ_E is the Euler–Mascheroni constant (we now explicitly write the non-dimensionalization for clarity). For comparison, in figure 4, we also show r_{sp} for a stokeslet between parallel plates as a single point with $a/h = 0$. We also note that the first term in the asymptotic expansion gives $r_{\text{sp}} \propto h$, which is the same scaling result as from the stokeslet model in §2.

We have simplified the full three-dimensional flow generated by the filter feeder to a two-dimensional model. This approach is a good first step in finding an analytical solution to the problem, and retains features from the stokeslet solution including an eddy size that increases with the separation between the no-slip boundaries. We expect the Brinkman equations to accurately model the true flow field, provided that the dimensionless permeability $k > 5$ (Tsay & Weinbaum 1991), i.e. when the gap thickness, $h \gtrsim 5.6a$ for $\beta = 0.16$. We expect this condition to be fulfilled in most experimental situations. However, the approximate nature of the boundary conditions applied at the feeder surface means that there may yet be quantitative differences between our Brinkman cylindrical model and the true three-dimensional flow field. We check for this in §4 using finite-element simulations to solve the full three-dimensional flow problem for a spherical cell body between two no-slip boundaries.

4. THREE-DIMENSIONAL SIMULATIONS

In order to analyse the effect of the approximations that were introduced in the Brinkman model and to model the influence of additional nearby boundaries upon the eddy size, we solve the full three-dimensional incompressible Stokes equation using finite-element analysis with Comsol MULTIPHYSICS software. We compare our simulations both with flow currents visualized in real filter feeders and with the predictions of the Brinkman model. To simulate the full three-dimensional flow field, we represent the three components of the velocity field by second-order elements, and use linear elements for the pressure field, p . The geometry for the simulation is shown in figure 1c. On the sphere, we specify $u_\theta = \sin \theta$ and $u_\rho = 0$ where ρ and θ are spherical variables measured from the y -axis as shown in figure 1c. Although we have used θ here in a slightly different definition from that in the two-dimensional calculation, we do not anticipate any confusion from the reader. The glass slides are represented by upper and lower no-slip boundaries. The right-hand and left-hand boundaries are open, and slip conditions are applied on the front and back boundaries, making the system periodic in this direction. We adjust the width of the chamber, w , and its length, b , to ensure that the effect of chamber size on the eddy radius is less than 1 per cent.

The eddy centre is found numerically by finding the location in the $z = h/2$ plane where $\mathbf{u} = \mathbf{0}$ (velocities are interpolated between nodes using cubic patches). Typical results are plotted in figure 4. Realistic boundary conditions produce feeding loci that agree very well

with our new analytical results, even when $a \approx h/2$, so that the feeder almost touches the top and bottom plates. We note that the three-dimensional simulation results, which have a symmetric boundary condition, quantitatively match best the asymmetric Brinkman flow result, but in trend match best the symmetric Brinkman flow result.

5. EXPERIMENTAL RESULTS

Experimental observations of closed eddies around the filter feeder *Vorticella convallaria* confirm predictions from our models. In our experiments, *V. convallaria* are cultured as in Ryu & Matsudaira (submitted) and transferred to a Petri dish for observation under the microscope (Leica DMIRM, 10 \times magnification). To trace the flow, the fluid near the *V. convallaria* of interest is seeded with 1 μm diameter polystyrene beads, and the motion of these beads is filmed at 100 frames per second. Similar flow-field measurements have been made but the effect of changing boundaries was not examined (Sleigh & Aiello 1972; Sleigh & Barlow 1976; Nagai *et al.* 2009).

We probe the effect of two different boundary configurations upon the eddies generated by the filter feeder. First, we observe *V. convallaria* anchored to the edge of a coverglass (Corning Labware and Equipment no. 1) between two slides, as illustrated schematically in figure 1*d*. The distance between slides, h , is varied from 140 ± 20 to $566 \pm 28 \mu\text{m}$. In a second set-up, we observe *V. convallaria* between two slides, a distance $h = 127 \pm 28 \mu\text{m}$ apart, with the *Vorticella* midway between the two slides and without the presence of an anchoring coverslip. In this configuration, the *Vorticella* stalk is anchored to the bottom slide, but bent so that the *Vorticella* body has the same orientation relative to the slides as in figure 1*d*. This situation is most analogous to our calculations and simulations because the only boundaries present are the top and bottom no-slip slide surfaces.

We use particle tracking velocimetry (PTV) software custom-written in Matlab to extract flow-field data from videos of feeding *V. convallaria*. Particles are tracked using POLYPARTICLETRACKER in Matlab using the method of Rogers *et al.* (2007). Velocities are then calculated from the displacement of particles between sequential frames. These velocities are then binned in the x and y directions, the velocities in each bin averaged and this average velocity assigned to the centre of the bin. While there are some areas where we cannot compute the velocity owing to lack of particles tracked (often near the centre of the eddy), we find that this method creates reliable flow fields for most of our data. We re-scale these data by dividing lengths by the radius of *V. convallaria* (determined as the maximum width of the *V. convallaria* body in the first video frame) and rotate tracks so that the long axis of the *V. convallaria* body is aligned with the y -axis for ease of comparison with calculations and simulations. We also centre the tracks so that the centre of the *V. convallaria* is at (0, 0) in the x - y plane.

The centres of the eddies are found based on an algorithm similar to that described in §4, where the

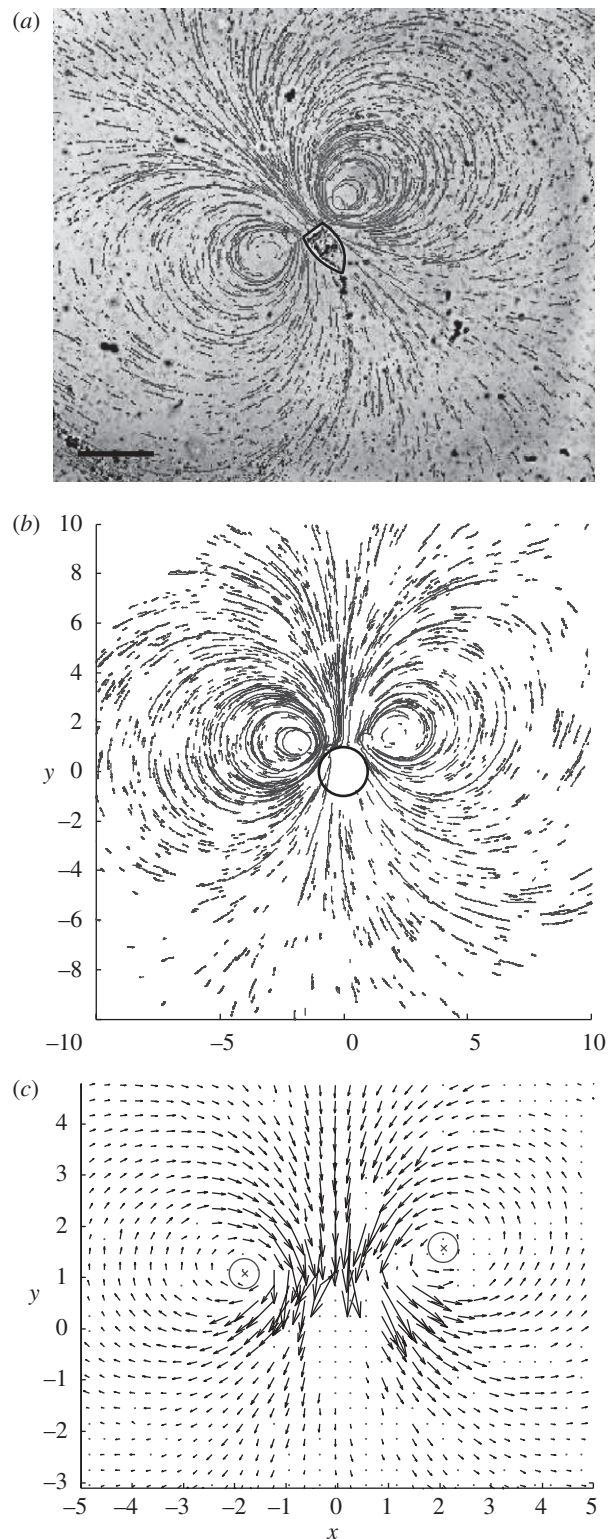


Figure 5. An example of the analysis of experimental data. (a) One frame from a high-speed movie showing a *V. convallaria* in the centre overlaid with particle tracks. The *Vorticella* body is outlined in a thick solid line. Scale bar, 100 μm . (b) The particle tracks from (a) rotated and scaled by the radius of the *Vorticella*. The circles show the position and radius of the *Vorticella*. (c) The flow field calculated by PTV. Velocities are scaled such that they will not intersect, and then lengthened by a further factor of four. The three largest velocity vectors have been removed for ease of viewing. X-marks surrounded by circles (grey) show the centre of the eddies with the outer circle representing the positional error. For this example, $h = 127 \pm 28 \mu\text{m}$.

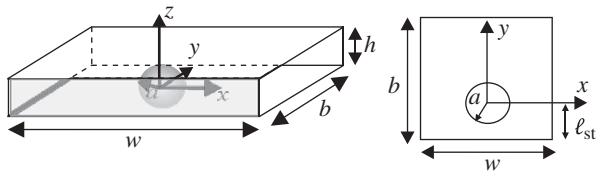


Figure 6. Simulation geometry for comparison with experiments. The upper and lower boundaries are no-slip. The right-hand and left-hand boundaries are open, and the front boundary is slip. The back boundary is no-slip, we emphasize this change from figure 1c by shading this boundary grey. This diagram is not to scale. In simulations and experiments, $a < \ell_{st} \ll w, b$.

velocity data are interpolated when necessary. An example of the full data analysis process is shown in figure 5.

In the experimental situation most analogous to our calculations and simulations, with the *Vorticella* midway between two slides and with $h = 127 \pm 28 \mu\text{m}$, we find $r_{sp}/h = 0.48 \pm 0.06$ (95% confidence interval, $N = 10$). This point is plotted in figure 4 for comparison with calculations and simulations. We find that this experiment agrees with the Brinkman model, confirming that the eddies seen in these experiments are due to the confining boundaries of the two slides parallel to the plane of view.

For our experiments where the *Vorticella* is anchored to the narrow side of a coverglass, as in figure 1d, the presence of this anchoring boundary must be taken into account in addition to the boundaries above and below the *Vorticella*. For this reason, we repeat the simulations as in §4, with the geometry modified so that there is a third no-slip boundary at $y = -\ell_{st}$, where the length ℓ_{st} represents the length of the *Vorticella* stalk. In our experiments, this length ranges from $\ell_{st}/a \approx 3$ to 5. The geometry for the simulation is shown in figure 6.

In order to collapse the eddies from cells at different sizes, with different coverglass separations, and different stalk lengths, we scale the eddy sizes measured from experiments and simulations by the eddy size, r_{sp}^l , for a sphere located above a single-plane boundary at $y = -\ell_{st}$, with the boundary condition of §4 imposed on the sphere and no additional boundaries present (figure 8). In the limit $\ell_{st}/h < 1$, asymptotic analysis gives $r_{sp}^l/\ell_{st} = 1.085 + 4.705(a/\ell_{st})^2$ (see appendix C).

When scaled appropriately, experimental and simulated data agree over a wide range of different cell body sizes, as shown in figure 7, which demonstrates that the size of the feeding eddies is controlled by the confining walls through which the flows are observed.

From figure 7, we can see that, for $h < r_{sp}^l$, the eddy size is well predicted by the stokeslet model, $r_{sp} = 0.44 h$ (shown as a solid line in figure 7). On the other hand, for $h \gtrsim r_{sp}^l$, the eddy size is well predicted by a model that accounts for the new no-slip boundary but neglects all other boundaries. In general, although we would intuitively expect that the eddy size is controlled by the distance to the closest boundary, it seems that the

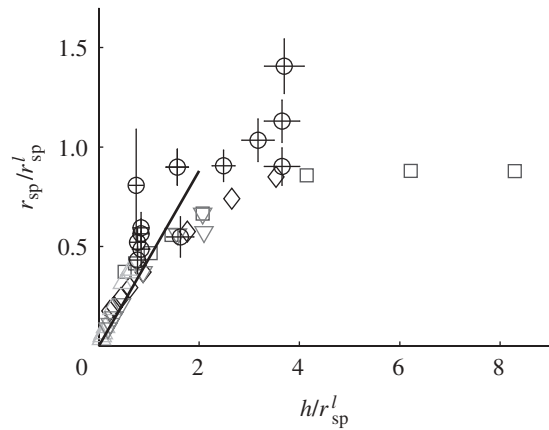


Figure 7. Plot of r_{sp}/r_{sp}^l versus h/r_{sp}^l for simulations (shapes) and experiments (circles), where r_{sp}^l is the predicted distance to the eddy centre for large h as described in the text. The solid line is the prediction $r_{sp} = 0.44 h$ from the stokeslet model. In experiments, ℓ_{st} was measured from the anchoring tip of the *Vorticella* stalk to the middle of the crown. In simulations, both h , the distance between top and bottom boundaries, and ℓ_{st} , the distance to the third no-slip boundary, were varied. Squares: $h/a = 2.5-40$, $\ell_{st}/a = 3$; diamonds: $h/a = 2.5-40$, $\ell_{st}/a = 10$; upward triangles: $h/a = 3$, $\ell_{st}/a = 1.5-50$; downward triangles: $h/a = 10$, $\ell_{st}/a = 1.5-50$.

system actually selects the smallest of the two possible eddy sizes (either from the anchoring wall or from the coverslips).

The large error bars on the experimental data are owing to errors inherent in measuring and centring the *V. convallaria* in digital images as well as to the interpolation necessary to locate the centres of these eddies. There is also some error in determining the distance between slides, h , which arises mainly from variation in manufacturing of the spacers that we use (either coverglasses of varying thickness, or paper spacers from the Hybaid EasiSeal system). We also do not account for drift of the *Vorticella* body out of the mid-plane, or for tilting of the body with respect to the tethering coverglass, although experiments were discarded if during filter feeding the *Vorticella* crown was pointed in the $\pm e_z$ direction. We believe that these variations account for most of the quantitative discrepancy between simulation and theory in figure 7. This leaves only a small residue of difference between the experimental measurements and the predictions of the model that must be attributed to the unmodelled effects of cell-body geometry and the location of the bands of cilia in real *Vorticella*.

6. CONCLUSION

We have derived and validated a hierarchy of models for the flow created by *Vorticella* between two parallel walls. Three-dimensional finite-element simulations agree in detail with the experiment. In the absence of an anchoring wall, as for instance when the cell is tethered to either of the coverslips, a Brinkman flow model is in good agreement with the simulations, and provides

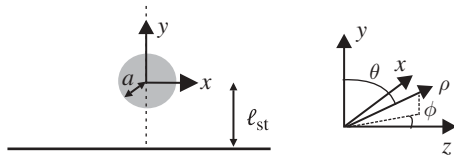


Figure 8. Schematic of geometry for sphere above plane boundary calculations. Dotted line represents an axis of symmetry.

an analytically tractable method for determining the effect of cell shape, and of the placement of cilia of the *Vorticella* upon the feeding currents.

We also explored a common experimental scenario, in which *Vorticella* is anchored to a wall, which provides a third confining boundary, in addition to the parallel boundaries representing the coverslips. Although in general all three nearby boundaries must be considered, we found that, over a wide range of experimental conditions, the two sets of boundaries produce eddies that are well separated in size. For this situation, the eddy size is determined by the minimum of the eddy sizes predicted when the two sets of boundaries are considered separately. Only when the two sets of boundary conditions independently give rise to eddies of approximately the same size must all boundaries be considered together when predicting the eddy size.

For experimentalists studying the flow around microscopic sessile filter feeders, caution should be used when observing closed feeding currents near boundaries. It is likely that these eddies are caused by the fact that the organism is applying a force to the fluid near a boundary and not by any particular motion of the organism under observation. As a guide to such experiments, we summarize the results of this work as a rule of thumb. For a sessile filter feeder anchored to a boundary perpendicular to the plane of view, eddies caused by boundaries will have a size approximately

$$r_{\text{sp}} \approx \begin{cases} 0.44 h & h \lesssim \ell_{\text{st}}(1 + 4.7(a/\ell_{\text{st}})^2), \\ \ell_{\text{st}}(1 + 4.7(a/\ell_{\text{st}})^2) & h \gtrsim \ell_{\text{st}}(1 + 4.7(a/\ell_{\text{st}})^2). \end{cases} \quad (6.1)$$

Without the presence of a perpendicular boundary, eddies caused by boundaries will have a size of approximately $0.44 h$. Only eddies of different length scales from those predicted above are likely to be caused by the specific action of the organism under observation. In particular, the distance between the organism and the coverslips through which the flow is observed should be at least 2.3 times the size of any observed eddy to ensure that the eddy is not a boundary artefact.

We have shown that the flow around filter feeders in nature will be quite different from that when examined under a microscope between two slides. Single filter feeders in nature may have much greater access to nutrients than predicted from experiments. For instance, observations of flow volumes and rates based on experiments in confined geometries (Sleigh & Barlow

1976; Nagai *et al.* 2009) are likely to significantly underestimate the values of such parameters in nature.

Although we have discussed the role of geometric confinement as a confounding factor when comparing experimentally observed feeding flows with the flow structures created by filter-feeding organisms in their natural environments, boundary-dominated flows may yet exist in nature. Filter feeders may find themselves either confined by the substrate to which they are anchored or crowded by neighbouring feeders. In general, nearby surroundings will strongly affect the flow generated by the filter feeder, and thus the feeding efficiency of the organism.

We thank Adam Abate for helpful discussion about PTV and Carl Meinart for emphasizing the use of the Brinkman approximation for microfluidic situations. We also thank the NSF and Harvard MRSEC (DMR-0820484). This research was partially funded by the National Science Foundation IGERT grant DGE no. 0221682. M.R. is supported by the Miller Institute for Basic Research in Sciences. S.R. and P.M. are supported by the Institute for Collaborative Biotechnologies through grant DAAD19-03-D-0004 from the US Army Research Office.

APPENDIX A: STOKESLET BETWEEN PARALLEL WALLS WITH PERIODIC BOUNDARY CONDITIONS

We follow Mucha *et al.* (2004) to numerically calculate the velocity field owing to a stokeslet between and parallel to no-slip walls with periodic boundary conditions (see figure 1a for a schematic view). The walls are separated by a distance, h , with a periodic length of w and b in the x and y directions, respectively. The stokeslet is located at $(0, 0, Z)$ and points in the e_y direction; we will later specify $Z = h/2$ to analyse the flow due to a stokeslet in the mid-plane.

The velocity, $\mathbf{U} = (u, v, w)$, is expanded in a Fourier series in the x and y directions, $\mathbf{U}(\mathbf{r}) = \sum_{\lambda} \hat{\mathbf{U}}(z) \exp(i\ell x + imy)$ with the summation over $\lambda = (\ell, m)$. The expansion in the Stokes equation yields

$$\frac{i\ell \hat{p}}{\mu} = \hat{u}_{zz} - (\ell^2 + m^2)\hat{u}, \quad (\text{A } 1)$$

$$\frac{im \hat{p}}{\mu} = \hat{v}_{zz} - (\ell^2 + m^2)\hat{v} + \frac{\delta(z - Z)}{(\mathcal{A}\mu)} \quad (\text{A } 2)$$

$$\text{and} \quad \frac{\hat{p}_z}{\mu} = \hat{w}_{zz} - (\ell^2 + m^2)\hat{w}, \quad (\text{A } 3)$$

where μ is the viscosity of the fluid and \mathcal{A} is the periodic area, $w \times b$. The continuity equation gives

$$i\ell \hat{u} + im \hat{v} + \hat{w}_z = 0. \quad (\text{A } 4)$$

We also specify $\hat{\mathbf{U}} = \mathbf{0}$ at $z = 0$ and $z = h$. Summing the z -derivative of equation (A 3) with equation (A 1) multiplied by $i\ell$ and equation (A 2) multiplied by im and combining and eliminating the velocities using the continuity equation gives

$$\hat{p}_{zz} - (\ell^2 + m^2)\hat{p} = \left(\frac{im}{\mathcal{A}}\right) \delta(z - Z). \quad (\text{A } 5)$$

This equation can be solved separately in the regions above and below the stokeslet. Below the stokeslet ($0 < z < Z$), we find

$$\left. \begin{aligned} \hat{u}_B &= A_2 \sinh(\lambda z) + \frac{i\ell z}{\lambda} [C_B \cosh(\lambda z) \\ &\quad + B_B \sinh(\lambda z)], \\ \hat{v}_B &= A_3 \sinh(\lambda z) + \frac{imz}{\lambda} [C_B \cosh(\lambda z) \\ &\quad + B_B \sinh(\lambda z)], \\ \hat{w}_B &= A_1 \sinh(\lambda z) + z[B_B \cosh(\lambda z) \\ &\quad + C_B \sinh(\lambda z)] \\ \text{and } \hat{p}_B &= 2\mu[B_B \cosh(\lambda z) + C_B \sinh(\lambda z)], \end{aligned} \right\} \quad (\text{A } 6)$$

where $\lambda = \sqrt{\ell^2 + m^2}$ and where we have used the velocity boundary condition to eliminate some terms. Combining the above with the continuity equation gives $B_B = -\lambda A_1$, $C_B = -i\ell A_2 - imA_3$. Above the stokeslet ($Z < z < h$), we find

$$\left. \begin{aligned} \hat{u}_A &= A_5 \sinh(\lambda z') + \frac{i\ell z'}{\lambda} [C_A \cosh(\lambda z') \\ &\quad + B_A \sinh(\lambda z')], \\ \hat{v}_A &= A_6 \sinh(\lambda z') + \frac{imz'}{\lambda} [C_A \cosh(\lambda z') \\ &\quad + B_A \sinh(\lambda z')], \\ \hat{w}_A &= A_4 \sinh(\lambda z') - z'[B_A \cosh(\lambda z') \\ &\quad + C_A \sinh(\lambda z')] \\ \text{and } \hat{p}_A &= 2\mu[B_A \cosh(\lambda z') + C_A \sinh(\lambda z')], \end{aligned} \right\} \quad (\text{A } 7)$$

where $z' = h - z$, and we have used the velocity boundary condition at $z = h$. Combining the above with the continuity equation, as before, gives $B_A = \lambda A_4$, $C_A = -i\ell A_5 - imA_6$. We next find the A_j coefficients by satisfying the conditions at $z = Z$: \hat{u}_z , \hat{v}_z , \hat{w}_z and \hat{p} are continuous. We also find, by integrating equations (A 1)–(A 3) and (A 5), that \hat{u}_z and \hat{w}_z are continuous while $\hat{v}_{Az}(Z) - \hat{v}_{Bz}(Z) = -1/(\mathcal{A}\mu)$ and $\hat{p}_{Az}(Z) - \hat{p}_{Bz}(Z) = im/\mathcal{A}$. We can solve for the A_j for a given λ and Z by combining these jump conditions with equations (A 6) and (A 7). The algebraic equations for the A_j can be found in table 1 of Mucha *et al.* (2004), with a change of variables ($d \rightarrow h$, $X \rightarrow Z$, $\eta \rightarrow \mu$ and $k \rightarrow \lambda$) to match the coordinates and conventions of our paper. Note that we believe there is a typographical error in Mucha *et al.* (2004) eqn (A 9) and that the equation for A_6 should be -2 multiplied by the current equation.

APPENDIX B: DETAILS OF BRINKMAN FLOW CALCULATIONS

To calculate the flow around a cylinder of radius a as in figure 1*b*, we solve the boundary value problem

$$\nabla^2 \mathbf{u} = \nabla p \quad \text{and} \quad \nabla \cdot \mathbf{u} = 0, \quad (\text{B } 1)$$

where we have scaled all lengths by a , velocities by u_0 and stresses by $\mu u_0/a$. For convenience, we define $\vartheta = \pi - \theta$. We also specify the boundary condition at

$r = 1$ of $u_\vartheta = \sin(n\vartheta)$, where $n \geq 1$ and is an integer, $u_r = 0$, and no-slip conditions on all other rigid boundaries ($z = \pm(1/2)(h/a)$) and at infinity. We work under the Brinkman approximation (Brinkman 1947; Tsay & Weinbaum 1991), which here amounts to $\partial^2 \mathbf{u}/\partial z^2 = -(\mathbf{u}/k)$, where $k \propto (h/a)^2$ is the permeability and the velocity is restricted to planes parallel to the boundaries, i.e. $\mathbf{u} = (u_r, u_\vartheta)$ and $u_z \equiv 0$. In a component form, we have

$$\left. \begin{aligned} \frac{\partial p}{\partial r} &= \frac{\partial}{\partial r} \left(\frac{1}{r} \frac{\partial}{\partial r} (r u_r) \right) + \frac{1}{r^2} \frac{\partial^2 u_r}{\partial \theta^2} - \frac{2}{r^2} \frac{\partial u_\theta}{\partial \theta} - \frac{u_r}{k} \\ \text{and} \\ \frac{1}{r} \frac{\partial p}{\partial \theta} &= \frac{\partial}{\partial r} \left(\frac{1}{r} \frac{\partial}{\partial r} (r u_\theta) \right) + \frac{1}{r^2} \frac{\partial^2 u_\theta}{\partial \theta^2} + \frac{2}{r^2} \frac{\partial u_r}{\partial \theta} - \frac{u_\theta}{k} \end{aligned} \right\} \quad (\text{B } 2)$$

and the continuity equation is

$$0 = \frac{1}{r} \frac{\partial}{\partial r} (r u_r) + \frac{1}{r} \frac{\partial u_\theta}{\partial \theta}. \quad (\text{B } 3)$$

Equations (B 2) and (B 3) are unchanged with the substitutions $u_\theta \rightarrow u_\vartheta$ and $\partial/\partial\theta \rightarrow \partial/\partial\vartheta$ as $u_\theta = -u_\vartheta$ and $\partial/\partial\theta = -(\partial/\partial\vartheta)$. Because of the form of the boundary conditions, we then seek

$$\left. \begin{aligned} u_r(r, \vartheta) &= U_r(r) \cos(n\vartheta), \\ u_\vartheta(r, \vartheta) &= U_\vartheta(r) \sin(n\vartheta), \\ \text{and } p(r, \vartheta) &= P(r) \cos(n\vartheta), \end{aligned} \right\} \quad (\text{B } 4)$$

which reduce the governing equations to

$$\left. \begin{aligned} \frac{dP}{dr} &= \frac{d}{dr} \left(\frac{1}{r} \frac{d}{dr} (r U_r) \right) - \frac{n^2}{r^2} U_r - \frac{2n}{r^2} U_\vartheta - \frac{U_r}{k}, \\ -\frac{nP}{r} &= \frac{d}{dr} \left(\frac{1}{r} \frac{d}{dr} (r U_\vartheta) \right) - \frac{n^2}{r^2} U_\vartheta - \frac{2n}{r^2} U_r - \frac{U_\vartheta}{k} \\ \text{and } nU_\vartheta &= -\frac{\partial}{\partial r} (r U_r). \end{aligned} \right\} \quad (\text{B } 5)$$

With a little algebra, we can eliminate U_ϑ and P in order to arrive at a single fourth-order ordinary differential equation for U_r

$$\mathcal{L}_n U_r + \frac{4}{r^2} U_r - \frac{1}{n^2} \frac{d}{dr} \left(r \mathcal{L}_n \frac{d}{dr} (r U_r) \right) = 0, \quad (\text{B } 6)$$

where the operator \mathcal{L}_n is defined as $\mathcal{L}_n = (d/dr)((1/r)(d/dr)(r \cdot)) - (n^2/r^2) - (1/k)$. The solution of this equation is

$$\begin{aligned} U_r(r) &= c_1 r^{n-1} + \frac{c_2}{r^{n+1}} \\ &\quad + \frac{1}{r} \left[c_3 K_n(r/\sqrt{k}) + c_4 I_n(r/\sqrt{k}) \right], \end{aligned} \quad (\text{B } 7)$$

where I_n and K_n are modified Bessel functions of order n . In order for the solution to be bounded as $r \rightarrow \infty$, we take $c_1 = c_4 = 0$.

From the continuity equation, we find $U_{\vartheta}(r)$ and from equation (B 2) we obtain the pressure field. Putting the details together, we have

$$\left. \begin{aligned} u_r(r, \vartheta) &= \left(\frac{c_2}{r^{n+1}} + \frac{c_3}{r} K_n \left(\frac{r}{\sqrt{k}} \right) \right) \cos(n\vartheta), \\ u_{\vartheta}(r, \vartheta) &= \left(\frac{c_2}{r^{n+1}} + \frac{c_3}{r} \left[K_n \left(\frac{r}{\sqrt{k}} \right) + \frac{r}{n\sqrt{k}} K_{n-1} \left(\frac{r}{\sqrt{k}} \right) \right] \right) \times \sin(n\vartheta) \end{aligned} \right\} \quad (\text{B } 8)$$

and $p(r, \vartheta) = \frac{c_2}{knr^n} \cos(n\vartheta)$.

At $r = 1$, we have $u_r = 0$ and $u_{\vartheta} = \sin \vartheta$ for all ϑ and k . Hence, we find

$$c_3 = -\frac{c_2}{K_n(1/\sqrt{k})} \quad \text{and} \quad c_2 = -\frac{n\sqrt{k}K_n(1/\sqrt{k})}{K_{n-1}(1/\sqrt{k})}. \quad (\text{B } 9)$$

We next evaluate the stream function for the motion in the plane. For cylindrical coordinates,

$$u_r(r, \vartheta) = \frac{1}{r} \frac{\partial \psi}{\partial \vartheta}, \quad u_{\vartheta}(r, \vartheta) = -\frac{\partial \psi}{\partial r}. \quad (\text{B } 10)$$

We then integrate the equations above to obtain

$$\psi(r, \vartheta) = \frac{\sqrt{k}K_n(1/\sqrt{k})}{K_{n-1}(1/\sqrt{k})} \left[-\frac{1}{r^n} + \frac{K_n(r/\sqrt{k})}{K_n(1/\sqrt{k})} \right] \sin(n\vartheta). \quad (\text{B } 11)$$

The streamlines for the $n = 1$ case are plotted in figure 2b.

We also find the position of the eddy centre as k approaches ∞ . The limiting behaviour of the modified Bessel function, $K_n(x)$, for $x \ll 1$ is (Jackson 1998)

$$K_n(x) \rightarrow \begin{cases} -\left[\ln \left(\frac{x}{2} \right) + \dots \right], & n = 0, \\ \frac{\Gamma(n)}{2} \left(\frac{2}{x} \right)^n, & n \neq 0. \end{cases} \quad (\text{B } 12)$$

From equation (B 8), we see that $u_r = 0$ when $\vartheta = \pi/2$, i.e. on the x -axis for all odd n . For odd n , the eddy centre lies on the x -axis at a radial position that satisfies

$$0 = \left(\frac{c_2}{r^{n+1}} + \frac{c_3}{r} \left[K_n \left(\frac{r}{\sqrt{k}} \right) + \frac{r}{\sqrt{k}} K_{n-1} \left(\frac{r}{\sqrt{k}} \right) \right] \right). \quad (\text{B } 13)$$

In the limit $k \gg 1$ we find $c_2/c_3 = -K_n(1/\sqrt{k}) = (-\Gamma(n)/2)(2\sqrt{k})^n$. Defining $s = r/\sqrt{k}$, equation (B 13) reduces to

$$\frac{(n-1)!2^{n-1}}{s^n} = K_n(s) + \frac{s}{n} K_{n-1}(s), \quad (\text{B } 14)$$

in the $k \gg 1$ limit, giving the position of the eddy centre at

$$r_{\text{sp}} = s\sqrt{k}. \quad (\text{B } 15)$$

We numerically find that, for $n = 1$, the symmetric boundary condition case, $s = 1.114$, satisfies equation (B 14). Further expansion of equation (B 13) for $n = 1$ gives a two-term approximation for the position of the eddy centre of

$$r_{\text{sp}} = 1.114\sqrt{k} + 1.14 \left(1 - 2\gamma_E - 2 \ln \frac{1}{2\sqrt{k}} \right) k^{3/2}, \quad (\text{B } 16)$$

where γ_E is the Euler–Mascheroni constant. Substituting $k = \beta(h/a)^2$, where β is a proportionality constant, and using dimensional variables yields

$$\frac{r_{\text{sp}}}{h} = 1.114\sqrt{\beta} + 1.14\beta^{-(1/2)} \left(1 - 2\gamma_E - 2 \ln \frac{a}{2\sqrt{\beta}h} \right) \left(\frac{a}{h} \right)^2, \quad (\text{B } 17)$$

which is plotted in figure 4 for two values of β .

APPENDIX C: SPHERE ABOVE A PLANE BOUNDARY

To calculate the flow around a sphere with radius a above a plane boundary as in figure 8, we solve the boundary value problem

$$\nabla^2 \mathbf{u} = \nabla p \quad \text{and} \quad \nabla \cdot \mathbf{u} = 0, \quad (\text{C } 1)$$

where we have scaled all lengths by a , velocities by u_0 and stresses by $\mu u_0/a$. We work in spherical coordinates with the sphere centred on the origin and the wall at $y = -\ell_{\text{st}}$. We enforce on the surface of the sphere ($\rho = 1$) $u_{\rho} = 0$ and $u_{\theta} = \sin \theta$ and at the wall $\mathbf{u} = \mathbf{0}$. We simplify the solution by noting that, in free space, a sphere with the above boundary conditions consists of a superposition of a stokeslet pointing in the $-\mathbf{e}_y$ direction and a point dipole of equal strength pointing in the opposite direction, both located at the centre of the sphere. Therefore, a sphere next to a plane with these boundary conditions can be approximated by superposing a stokeslet and its image system with a point dipole and its image system.

In this section, we will work with the stream functions in spherical axially symmetric coordinates for simplicity. In these coordinates, we have

$$u_{\rho} = \frac{1}{\rho^2} \frac{\partial \psi}{\sin \theta \partial \theta}, \quad u_{\theta} = -\frac{1}{\rho \sin \theta} \frac{\partial \psi}{\partial \rho}, \quad (\text{C } 2)$$

and equation (C 1) reduces to $E^4 \psi = 0$, where $E^4 = E^2 \circ E^2$ and

$$E^2 = \frac{\partial^2}{\partial \rho^2} + \frac{1}{\rho^2} \sin \theta \frac{\partial}{\partial \theta} \left(\frac{1}{\sin \theta} \frac{\partial}{\partial \theta} \right). \quad (\text{C } 3)$$

A stokeslet at the origin oriented in $-\mathbf{e}_y$ direction gives

$$\psi^S(\rho, \theta) = \rho \sin^2 \theta. \quad (\text{C } 4)$$

The potential dipole can be derived as $\psi^D = -(1/2)E^2 \psi^S$ (Chwang & Wu 1975, p. 791) yielding

$$\psi^D(\rho, \theta) = \frac{\sin^2 \theta}{\rho}. \quad (\text{C } 5)$$

For a sphere with boundary condition $u_\theta = \sin\theta$ we have

$$\psi^{\text{SPH}}(\rho, \theta) = \frac{1}{2}\psi^{\text{S}}(\rho, \theta) - \frac{1}{2}\psi^{\text{D}}(\rho, \theta). \quad (\text{C } 6)$$

We must now consider the image system for these singularities. The solution for a stokeslet above a no-slip boundary is well known to be the solution for the original stokeslet in free space plus an image system consisting of a stokeslet, a source dipole and a stokeslet doublet (Blake 1971; Blake & Chwang 1974; Pozrikidis 1992)

$$\psi^{\text{SW}}(\rho, \mu, \ell_{\text{st}}) = \psi^{\text{S}}(\rho, \mu) - \psi^{\text{S}}(\rho_{\text{im}}, \mu_{\text{im}}) + 2\ell_{\text{st}}^2\psi^{\text{D}}(\rho_{\text{im}}, \mu_{\text{im}}) - 2\ell_{\text{st}}\psi^{\text{SD}}(\rho_{\text{im}}, \mu_{\text{im}}), \quad (\text{C } 7)$$

where we use $\mu = \cos\theta$ for convenience and where $\rho_{\text{im}} = \sqrt{\rho^2(1 - \mu^2) + (\rho\mu + 2\ell_{\text{st}})^2}$ is the radial distance measured from the image position and $\mu_{\text{im}} = (2\ell_{\text{st}} + \rho\mu) / \left(\sqrt{(2\ell_{\text{st}} + \rho\mu)^2 + \rho^2(1 - \mu^2)} \right)$ is based on the angle measured from the image position. The images are located on the axis at $y = -2\ell_{\text{st}}$. Similarly, the stream function for a potential dipole above a wall is

$$\psi^{\text{DW}}(\rho, \mu, \ell_{\text{st}}) = \psi^{\text{D}}(\rho, \mu) - 3\psi^{\text{D}}(\rho_{\text{im}}, \mu_{\text{im}}) + 2\ell_{\text{st}}\psi^{\text{Q}}(\rho_{\text{im}}, \mu_{\text{im}}) - 2\psi^{\text{SQ}}(\rho_{\text{im}}, \mu_{\text{im}}), \quad (\text{C } 8)$$

where ψ^{Q} and ψ^{SQ} are the stream functions for a potential quadrupole and Stokes quadrupole, respectively, and

$$\left. \begin{aligned} \psi^{\text{SD}}(\rho, \mu) &= \mu - \mu^3, \\ \psi^{\text{SQ}}(\rho, \mu) &= -\frac{(3\mu^4 - 4\mu^2 + 1)}{\rho} \\ \text{and} \quad \psi^{\text{Q}}(\rho, \mu) &= \frac{3\mu(\mu^2 - 1)}{\rho^2}. \end{aligned} \right\} \quad (\text{C } 9)$$

The above equations can be derived from equations (C 4) and (C 5) by noting that the next multipole/multiplet in the series can be derived by taking $(\mathbf{f} \cdot \nabla)\psi$, where ψ is the previous multipole/multiplet and \mathbf{f} is the unit direction of the new multipole/multiplet (Chwang & Wu 1975). For instance, $\psi^{\text{SD}}(\rho, \mu) = (\mathbf{f} \cdot \nabla)\psi^{\text{S}}(\rho, \mu)$. In our case $\mathbf{f} = -\mathbf{e}_y = -\cos\theta\mathbf{e}_\rho + \sin\theta\mathbf{e}_\theta$ and $(\mathbf{f} \cdot \nabla)\psi = -\cos\theta(\partial/\partial\rho) + (\sin\theta/\rho)(\partial/\partial\theta) = -\mu(\partial/\partial\rho) - (1 - \mu^2)/\rho(\partial/\partial\mu)$.

For a sphere of radius $\rho = 1$ at height ℓ_{st} above a no-slip wall with $u_\theta = 0$ and $u_\rho = 0$ at the surface of the sphere, we have an approximation of

$$\psi(\rho, \theta, \ell_{\text{st}}) = C(\ell_{\text{st}})[\psi^{\text{SW}}(\rho, \theta) - \psi^{\text{DW}}(\rho, \theta)], \quad (\text{C } 10)$$

where

$$C(\ell_{\text{st}}) = -\frac{(4\ell_{\text{st}}^2 + 1)^{7/2}}{2\left(-96\ell_{\text{st}}^6 + 20\ell_{\text{st}}^4 - 23\ell_{\text{st}}^2 + (4\ell_{\text{st}}^2 + 1)^{7/2} - 1\right)}. \quad (\text{C } 11)$$

This approximation satisfies the no-slip boundary condition at $y = -\ell_{\text{st}}$ without error, but has errors of order $1/\ell_{\text{st}}$ and $(1/\ell_{\text{st}})^2$ for u_ρ and u_θ , respectively, on the surface of the sphere, which could be corrected by adding further image terms.

To find the position of the eddy centre, r_{sp}^l , we solve two simultaneous equations $u_\rho = 0$ and $u_\theta = 0$. The velocity components can be calculated by combining equation (C 2) with equation (C 10). While these equations are complex, they yield a simple asymptotic expansion for $1/\ell_{\text{st}} \ll 1$,

$$\frac{r_{\text{sp}}^l}{\ell_{\text{st}}} = 1.085 + 4.705\left(\frac{1}{\ell_{\text{st}}}\right)^2. \quad (\text{C } 12)$$

REFERENCES

- Blake, J. R. 1971 A note on the image system for a stokeslet in a no-slip boundary. *Math. Proc. Camb. Philos. Soc.* **70**, 303–310. (doi:10.1017/S0305004100049902)
- Blake, J. & Chwang, A. 1974 Fundamental singularities of viscous flow. *J. Eng. Math.* **8**, 23–29. (doi:10.1007/BF02353701)
- Blake, J. R. & Otto, S. R. 1996 Ciliary propulsion, chaotic filtration and a ‘blinking’ stokeslet. *J. Eng. Math.* **30**, 151–168. (doi:10.1007/BF00118828)
- Blake, J. R., Liron, N. & Aldis, G. K. 1982 Flow patterns around ciliated microorganisms and in ciliated ducts. *J. Theor. Biol.* **98**, 127–141. (doi:10.1016/0022-5193(82)90062-5)
- Brinkman, H. C. 1947 A calculation of the viscosity and the sedimentation constant for solutions of large chain molecules taking into account the hampered flow of the solvent through these molecules. *Physica* **13**, 447–448. (doi:10.1016/0031-8914(47)90030-X)
- Chen, S. et al. 2004 The activated-sludge fauna and performance of five sewage treatment plants in Beijing, China. *Eur. J. Protistol.* **40**, 147–152. (doi:10.1016/j.ejop.2004.01.003)
- Christensen-Dalsgaard, K. K. & Fenchel, T. 2003 Increased filtration efficiency of attached compared to free-swimming flagellates. *Aquat. Microb. Ecol.* **33**, 77–86. (doi:10.3354/ame033077)
- Chwang, A. T. & Wu, T. Y. T. 1975 Hydromechanics of low-Reynolds-number flow. Part 2. Singularity method for Stokes flows. *J. Fluid Mech.* **67**, 787–815. (doi:10.1017/S0022112075000614)
- Drescher, K., Leptos, K. C., Tuval, I., Ishikawa, T., Pedley, T. J. & Goldstein, R. E. 2009 Dancing volvox: hydrodynamic bound states of swimming algae. *Phys. Rev. Lett.* **102**, 168101. (doi:10.1103/PhysRevLett.102.168101)
- Fenchel, T. 1982 Ecology of heterotrophic microflagellates. IV. Quantitative occurrence and importance as bacterial consumers. *Mar. Ecol. Prog. Ser.* **9**, 35–42. (doi:10.3354/meps009035)
- Fernandez, J., Kurowski, P., Petitjeans, P. & Meiburg, E. 2002 Density-driven unstable flows of miscible fluids in a Hele–Shaw cell. *J. Fluid Mech.* **451**, 239–260.
- Hartmann, C., Ozlemzmutlu, O., Petermeier, H., Fried, J. & Delgado, A. 2007 Analysis of the flow field induced by the sessile peritrichous ciliate *Opercularia asymmetrica*. *J. Biomech.* **40**, 137–148. (doi:10.1016/j.jbiomech.2005.11.006)
- Ishikawa, T. & Pedley, T. J. 2008 Coherent structures in monolayers of swimming particles. *Phys. Rev. Lett.* **100**, 088103. (doi:10.1103/PhysRevLett.100.088103)

- Jackson, J. D. 1998 *Classical electrodynamics*, p. 116, 3rd edn. New York, NY: Wiley.
- Kankaala, P. & Eloranta, P. 1987 Epizooic ciliates (*Vorticella* sp.) compete for food with their host *Daphnia longispina* in a small polyhumic lake. *Oecologia* **73**, 203–206. (doi:10.1007/BF00377508)
- King, N. 2005 Choanoflagellates. *Curr. Biol.* **15**, R113–R114. (doi:10.1016/j.cub.2005.02.004)
- Labarbera, M. 1984 Feeding currents and particle capture mechanisms in suspension feeding animals. *Am. Zool.* **24**, 71–84.
- Laybourn, J. 1976 Energy budgets for *Stentor coeruleus* Ehrenberg (Ciliophora). *Oecologia* **22**, 431–437. (doi:10.1007/BF00345319)
- Liron, N. & Blake, J. R. 1981 Existence of viscous eddies near boundaries. *J. Fluid Mech.* **107**, 109–129.
- Liron, N. & Mochon, S. 1976 Stokes flow for a stokeslet between two parallel flat plates. *J. Eng. Math.* **10**, 287–303. (doi:10.1007/BF01535565)
- Magar, V., Goto, T. & Pedley, T. J. 2003 Nutrient uptake by a self-propelled steady squirmer. *Quart. J. Mech. Appl. Math.* **56**, 65–91. (doi:10.1093/qjmam/56.1.65)
- Mucha, P. J., Tee, S. Y., Weitz, D. A., Shraiman, B. I. & Brenner, M. P. 2004 A model for velocity fluctuations in sedimentation. *J. Fluid Mech.* **501**, 71–104. (doi:10.1017/S0022112003006967)
- Nagai, M., Oishi, M. I., Oshima, M., Asai, H. & Fujita, H. 2009 Three-dimensional two-component velocity measurement of the flow field induced by the *Vorticella picta* microorganism using a confocal microparticle image velocimetry technique. *Biomicrofluidics* **3**, 014105. (doi:10.1063/1.3105106)
- Noland, L. E. & Finley, H. E. 1931 Studies on the taxonomy of the genus *Vorticella*. *Trans. Am. Micros. Soc.* **50**, 81–123. (doi:10.2307/3222280)
- Orme, B. A. A., Blake, J. R. & Otto, S. R. 2003 Modelling the motion of particles around choanoflagellates. *J. Fluid Mech.* **475**, 333–355.
- Petermeier, H., Kowalczyk, W., Delgado, A., Denz, C. & Holtmann, F. 2007 Detection of microorganismic flows by linear and nonlinear optical methods and automatic correction of erroneous images artefacts and moving boundaries in image generating methods by a neuronumerical hybrid implementing the Taylor's hypothesis as a priori knowledge. *Exp. Fluids* **42**, 611–623. (doi:10.1007/s00348-007-0269-3)
- Pettitt, M. E., Orme, B. A. A., Blake, J. R. & Leadbeater, B. S. C. 2002 The hydrodynamics of filter feeding in choanoflagellates. *Eur. J. Protistol.* **38**, 313–332. (doi:10.1078/0932-4739-00854)
- Pozrikidis, C. 1992 *Boundary integral and singularity methods for linearized viscous flow*, pp. 22 and 84. Cambridge, UK: Cambridge University Press.
- Rapport, D. J., Berger, J. & Reid, D. B. W. 1972 Determination of food preference of *Stentor coeruleus*. *Biol. Bull.* **142**, 103–109. (doi:10.2307/1540249)
- Reid, R. 1969 Fluctuations in populations of 3 *Vorticella* species from an activated-sludge sewage plant. *J. Protozool.* **16**, 103–111.
- Rogers, S. S., Waigh, T. A., Zhao, X. & Lu, J. R. 2007 Precise particle tracking against a complicated background: polynomial fitting with Gaussian weight. *Phys. Biol.* **4**, 220–227. (doi:10.1088/1478-3975/4/3/008)
- Rubenstein, D. I. & Koehl, M. A. R. 1977 The mechanisms of filter feeding: some theoretical considerations. *Am. Nat.* **111**, 981–994. (doi:10.1086/283227)
- Ryu, S. & Matsudaira, P. T. Submitted. Unsteady motion, finite reynolds number and wall effects on *Vorticella convallaria* contribute contraction force greater than the stokes drag. *Biophys. J.*
- Sherr, E. & Sherr, B. 1988 Role of microbes in pelagic food webs: a revised concept. *Limnol. Oceanogr.* **33**, 1225–1227.
- Short, M. B., Solari, C. A., Ganguly, S., Powers, T. R., Kessler, J. O. & Goldstein, R. E. 2006 Flows driven by flagella of multicellular organisms enhance long-range molecular transport. *Proc. Natl Acad. Sci. USA* **103**, 8315–8319. (doi:10.1073/pnas.0600566103)
- Sleigh, M. A. & Aiello, E. 1972 The movement of water by cilia. *Acta Protozool.* **11**, 265–277.
- Sleigh, M. A. & Barlow, D. 1976 Collection of food by *Vorticella*. *Trans. Am. Micros. Soc.* **95**, 482–486. (doi:10.2307/3225140)
- Tsay, R. Y. & Weinbaum, S. 1991 Viscous flow in a channel with periodic cross-bridging fibres: exact solutions and Brinkman approximation. *J. Fluid Mech.* **226**, 125–148.